Soft Matter

Accepted Manuscript

This article can be cited before page numbers have been issued, to do this please use: T. Su, J. Liu, D. Terwagne, P. Reis and K. Bertoldi, *Soft Matter*, 2014, DOI: 10.1039/C4SM00952E.

ROYAL SOCIETY OF CHEMISTRY

www.rsc.org/softmatter

View Article Online
DOI: 10.1039/C4SM00952E

ARTICLE TYPE

Buckling of an elastic rod embedded on an elastomeric matrix: planar vs. non-planar configurations

Tianxiang Su,[a,b] † **Jia Liu,**[a] † **Denis Terwagne,**[c,d] † **Pedro M. Reis,**[*c,e] **and Katia Bertoldi**[*a,f]

a: School of Engineering and Applied Sciences, Harvard University, Cambridge, MA, 02138, USA;
b: Current address: Schlumberger-Doll Research Center, Cambridge, MA, 02139, USA;
c: Department of Civil and Environmental Engineering, Massachusetts Institute of Technology, Cambridge, MA, 02139, USA;
d: Current address: Faculté des Sciences, Université Libre de Bruxelles (ULB), Bruxelles 1050, Belgium;
e: Department of Mechanical Engineering, Massachusetts Institute of Technology, Cambridge, MA, 02139, USA;
f: Kavli Institute for Bionano Science and Technology, Harvard University, Cambridge, MA, 02138, USA;
†: These authors contributed equally to this work;
*: To whom correspondence may be addressed: preis@mit.edu & bertoldi@seas.harvard.edu.

We investigate the buckling of a slender rod embedded in a soft elastomeric matrix through a combination of experiments, numerics and theory. Depending on the control parameters, both planar wavy (2D) or non-planar coiled (3D) configurations are observed in the post-buckling regime. Our analytical and numerical results indicate that the rod buckles into 2D configurations when the compression forces associated to the two lowest critical modes are well separated. In contrast, 3D coiled configurations occur when the two buckling modes are triggered at onset, nearly simultaneously. We show that the separation between these two lowest critical forces can be controlled by tuning the ratio between the stiffness of the matrix and the bending stiffness of the rod, thereby allowing for specific buckling configurations to be target by design.

1 Introduction

A slender fiber can buckle under axial compression even when embedded, and therefore supported, inside an elastomeric matrix [1–3]. As a result, planar periodic configurations (2D) have been observed in microtubules [4,5], fiber-reinforced composites [6–8], and pipelines on seabeds [9,10]. Non-planar coiled configurations (3D) have also been observed from the buckling of other constrained rodlike structures, including: plant roots growing in soil [11], packaged DNA in viruses [12], and coil tubing in oil-field operations [13,14]. Interestingly, it has recently been shown that a silicon nano-wire attached to a soft substrate [15] can exhibit either planar or non-planar configurations, depending on the stiffness of the substrate, which can be tuned. Finding both 2D and 3D configurations in the same system raises the fundamental question regarding the conditions under which an embedded fiber can buckle in-plane or out-of-plane. From a practical perspective, modern nano-devices that include rodlike components can be used for sensors, resonators and electromagnetic wave absorbers [16–18]. Rationalizing the post-buckling regime in this class of embedded filamentary structures could therefore open opportunities for functionality by generating complex 3D shapes, reversibly and on-demand.

Here, we investigate the mechanical response, under compression, of a single elastic fiber (rod) embedded in an elastomeric matrix. We seek to rationalize the conditions under which either planar or non-planar buckling configurations are attained, depending on the combined stiffnesses of the matrix and the rod. Throughout, we assume that no delamination occurs between the rod and the matrix. We start by performing precision model experiments where a Nitinol rod is embedded within a Polydimethylsiloxane (PDMS) cylinder, and the ensemble is compressed uniaxially. Our experiments reveal that for matrices that are sufficiently stiff (with respect to the bending stiffness of the rod) the rod buckles directly onto a non-planar coiled configuration. By contrast, with softer matrices, both 2D and 3D buckling configurations can be observed. Moreover, we find that the morphology of the buckled patterns and their associated characteristic length scales can be tuned by changing the geometric and material parameters of the system. These results are rationalized by a model based on the classic Winkler foundation [19]. Our analysis suggests that non-planar configurations are triggered when the critical buckling loads associated to the first two eigenmodes become comparable. This hypothesis is tested numerically by performing both dynamic simulations and finite element analyses. The simulations confirms that the separation between the two lowest critical loads determines whether a rod buckles in-plane or out-of-plane. Moreover, the numerical results highlight the important effect of the boundary conditions and the presence of shear deformation in the matrix in setting the observed buckling patterns.

View Article Online
DOI: 10.1039/C4SM00952E

2 Experiments

2.1 Experimental setup

In Fig. 1 we present a photograph of the experimental apparatus that we used to uniaxially compress our samples. Each sample consisted of a slender Nitinol rod that was concentrically embedded inside an elastomeric cylinder (the matrix) made out of Polydimethylsiloxane (PDMS). We fabricated, characterized and tested a total of 15 samples for which we changed the stiffness of the matrix, as well as as the radius and length of the rod (see Table S1 for detailed geometric and material properties). Upon compression, the Nitinol rod buckled within the matrix and the process was imaged by two perpendicular digital cameras. Representative configurations from the two orthogonal views are shown in the insets of Fig. 1.

Each experimental sample contained a SE508 Nitinol rod that is 10 cm long. At both ends of the sample, the rod was made to pass through a tight clearance hole centered on an acrylic disk, onto which it was glued, which ensured clamped boundary conditions. We used five Nitinol rods with radii and Young's moduli in the ranges $25.4 < r_r\ [\mu\text{m}] < 127$, and $59 < E_r\ [\text{GPa}] < 78$, respectively (see SI for exact values). Nitinol is known for its unique hyperelastic and shape memory properties[20,21]. Given that all experiments were performed at constant room temperature, $T = 20\,^\circ\text{C}$, we did not make use of its shape memory characteristics. Hyperelasticity, on the other hand, was important since it confers reversibility to the experimental tests, even for the geometrically nonlinear configurations observed in the post-buckling regime.

The elastomeric matrix (10 cm long and 2.6 cm in diameter) was cast on a cylindrical mold using PDMS (Sylgard 184 from Dow Corning Inc.), with the Nitinol rod held in between the two acrylic disks, along the central axis. Using PDMS had the advantage that its Young's modulus can be tuned during fabrication by varying the relative mixture of base and curing agents, from 0.4kPa to 3MPa[22] (see Fig. S1). In our experiments, however, we focused on the range $17 < E_m\,[\text{kPa}] < 84$, which enabled us to fully explore the post-buckling regime of the rod under compression, while preventing delimitation between the Nitinol and the PDMS matrix. Moreover, this range ensured that the samples could be supported horizontally, without significant deflection under their own weight.

Once fabricated, the samples were mechanically tested on a custom-made uniaxial compression device (Fig. 1). Each sample was laid horizontally on top of a series of five independent acrylic braces that were set perpendicular to the axis of compression (see inset of Fig. 1). These braces supported the sample and could slide along the axis of compression using two PTFE (Polytetrafluoroethylene) linear guides. A computer controlled linear stage uniaxially compressed the whole sample (matrix, rod and acrylic disks). Each test was performed quasi-statically under conditions of controlled displacement. Note that our setup differs from a previous study[23], where only the rod, without the matrix, was compressed.

During each experimental test, two perpendicular digital cameras were synchronized to acquire images of the Nitinol rods (one from the side and the other from above, as shown in Fig. 1) at every 0.1 mm step of compression. The pairs of frames were then combined and image-processed to produce 3D reconstructions of the coordinates of the rod. Two representative examples of the reconstructed configurations rods in the planar and non-planar regimes are presented in Fig. 2A and B, respectively. From the 3D reconstructions we could readily measure the wavelength of the buckled configurations, as well as the pitch of the non-planar shapes. Moreover, to further facilitate the analysis (described in more detail below), we also performed a Principal Component Analysis (PCA)[24,25] that rigidly rotates the configuration of the rod, without distortion, such that its major lateral buckling direction is always aligned with the global horizontal y-axis.

2.2 Experimental results

Both 2D and 3D buckling configurations of the Nitinol rod were observed during the uniaxial compression of our samples. In Fig. 2A and B, we present two representative configurations obtained for samples #1 and #2 (see Table S1), respectively, at $\varepsilon = 3\%$ compressive strain. Sample #1 buckled into a periodic planar configuration, whereas sample #2 buckled into a non-planar configuration, with deformation in the two orthogonal lateral directions.

The buckling shapes of each sample are further characterized by computing the ellipse of minimum area that encloses the cross-sectional view of the buckled rod at $\varepsilon = 3\%$ (dashed line in the cross-section views in Fig. 2A and B, see SI for details). The aspect ratio, b/a, between the minor and major axes of this ellipse, quantifies the extent to which the buckled shape is 2D or 3D. A flat ellipse ($b/a \ll 1$) indicates a planar configuration, while a more circular one ($b/a \sim 1$) indicates that it is fully 3D.

In Fig. 3A, we report the aspect ratio, b/a, for all 15 samples, as a function of their dimensionless matrix stiffness (rationalized in detail in §3, below),

$$\eta = \frac{E_m L_r^4}{E_r I_r}, \tag{1}$$

where E_m is the Young's modulus of the matrix and E_r, I_r and L_r are the Young's modulus, second moment of area and length of the rod, respectively. The experimental results reveal that: (*i*) For stiff matrices ($\eta > 5 \cdot 10^6$) all samples are characterized by large values of b/a, indicating a coiled, non-planar buckling shape; (*ii*) For $\eta < 5 \cdot 10^6$, both small and large values for b/a are observed, indicating that both planar

View Article Online
DOI: 10.1039/C4SM00952E

and non-planar configurations can occur. Whereas the finding (*ii*) is consistent with previous qualitative observations for a nanowire attached to a soft substrate[15], the finding (*i*) is, to the best of our knowledge, reported here for the first time.

We proceed by quantifying the wavelength, λ, of the buckled configurations, which we plot in Fig. 3B for all samples as a function of the dimensionless matrix stiffness, η, at $\varepsilon = 3\%$ compressive strain. Interestingly, the results for both planar and non-planar buckling configurations collapse onto the same curve that is consistent with a power-law $\lambda \sim \eta^{-1/4}$, which we will show in §3 can be rationalized and derived analytically.

Summarizing the experimental results thus far, we have found that the dimensionless stifness $\eta = E_m L_r^4/(E_r I_r)$ determines whether the rod buckles into a planar or a non-planar configuration and it also sets the characteristic length scales of the buckling pattern. We now seek to rationalize these results and proceed by investigating the effect that the stiffness of the matrix has on the mechanical response of the system, first analytically (§3) and later numerically (§4). The important role played by the boundary conditions will then be discussed in more detail in §5.

3 Theoretical analysis

Towards rationalizing the conditions that lead to 2D and 3D buckling configurations, we adopt the Winkler foundation model[19] of a thin and stiff beam supported by a softer elastic substrate. Moreover, the treatment of our elastomeric matrix is simplified as an array of springs with stiffness K acting solely in radial direction.

Assuming small strains and moderate rotations, the governing equation for the embedded elastic rod is given by[19],

$$E_r I_r \frac{\partial^4 Y}{\partial S^4} + F \frac{\partial^2 Y}{\partial S^2} + KY = 0, \tag{2}$$

where F is the applied compressive force and Y and S denote the lateral displacement and the arc length of the rod, respectively. Introducing the normalized displacement, $y = Y/L_r$, and arc length, $s = S/L_r$, allows for Eq. (2) to be rewritten in dimensionless form,

$$\frac{\partial^4 y}{\partial s^4} + \pi^2 f \frac{\partial^2 y}{\partial s^2} + \pi^4 k y = 0, \tag{3}$$

where $f = FL_r^2/(\pi^2 E_r I_r)$ and $k = KL_r^4/(\pi^4 E_r I_r)$ are the dimensionless compressive force and spring constant, respectively. When both ends of the rod are free to rotate, the solution of Eq. (3) has the form $y(s) = A\sin(n\pi s)$, with n denoting the mode number.

Substituting $y(s)$ into Eq. (3), yields the the compressive force required to trigger the n-th mode[19],

$$f_n = n^2 + \frac{k}{n^2}, \tag{4}$$

which can be alternatively obtained using an energy approach[26,27](see SI for details). Given that the mode associated to the lowest f_n emerges and grows during loading, the critical buckling force for the system is given by,

$$f_{\rm cr} = \min_{n=1,2,\cdots} \left(n^2 + \frac{k}{n^2} \right). \tag{5}$$

Even if this result is well known in the literature, we turn our focus to the fact for specific values of k, there can be two possible modes associated to f_{cr}. In Fig. 4A, we further highlight this point by plotting the dependence of the dimensionless difference, $\Delta f/f_{cr} = (f_{n'} - f_{cr})/f_{cr}$, between the lowest ($f_{cr}$) and second lowest ($f_{n'}$) compressive forces, as a function of k. We find that for the specific values of the normalized spring constant,

$$k = m^2(m+1)^2, \quad m = 1,2,3,... \tag{6}$$

$\Delta f/f_{cr}$ vanishes, such that the system is degenerated and two different modes, m and $m+1$ say, are both associated with the same critical compressive force, $f_{cr} = f_m = f_{m+1}$. As a result, two buckling modes are triggered simultaneously at the onset of instability and we expect them to interact with one another[28] to produce non-planar (3D) configurations.

The above interpretation is supported by our experimental results since in all cases of 3D coiled configurations, two neighboring modes were observed to grow in perpendicular directions. For example, the configuration shown in Fig. 2B exhibits the orthogonal modes $m = 2$ and $m = 3$, simultaneously. In contrast, when k is far from the specific values given by Eq. (6), the critical forces for adjacent modes are sufficiently separated such that only a single mode is expected to be triggered and grow, resulting in a 2D planar buckling configuration. It is also interesting to note that the maxima of $\Delta f/f_{cr}$ plotted in Fig. 4A decrease for increasing values of k. Consequently, rods embedded in stiff matrices are expected to always buckle into non-planar configurations, which is also consistent with the experimental results reported in Fig. 3A (for $\eta > 5 \cdot 10^6$).

The relation between our analysis and the experimental results can now be made more quantitative. We make use of existing results for the spring stiffness[6,7],

$$K = \frac{16\pi G_m(1-\nu_m)}{2(3-4\nu_m)K_0(n\pi r_r/L_r) + n\pi r_r K_1(n\pi r_r/L_r)/L_r}, \tag{7}$$

arising when a rod of radius r_r and length L_r buckles into mode n inside a matrix with shear modulus $G_m = E_m/[2(1+\nu_m)]$, where $K_0(\cdot)$ and $K_1(\cdot)$ are the modified Bessel functions and E_m and ν_m are the and Young's modulus and Poisson's ratio of the matrix, respectively. In the limit of a slender rod, *i.e.* $r_r/L_r \to 0$, Eq. (7) can be further simplified (see SI for details) to

$$K = \frac{8\pi G_m(1-\nu_m)}{\ln(2L_r/nr_r)}, \tag{8}$$

View Article Online
DOI: 10.1039/C4SM00952E

which has been recently used to study buckling of confined microtubules (assuming $\nu_m = 0.5$)[5].

Eqs. (7) and (8) indicate that K depends on both G_m and n, suggesting that attaining a general description for all buckling modes may be challenging. However, a unique relation between the wavelength of the mode, $\lambda = 2L_r/n$, and the spring and matrix stiffness can indeed be determined upon calculation of the mode number that minimize f_n (*i.e.* determining the values of n for which $\partial f_n/\partial n = 0$). In particular, minimization of f_n using Eq. (8) yields,

$$\frac{(\lambda/L_r)^4\,(2\ln(\lambda/r_r)-1)}{[\ln(\lambda/r_r)]^2} = \frac{24\pi^3}{\eta}, \qquad (9)$$

where $\eta = E_m L_r^4/E_r I_r$ is the dimensionless stiffness of the matrix introduced earlier in Eq. (1). Eq. (9) can be solved iteratively to obtain λ for a given set of matrix and rod properties.

This analysis reveals that λ depends on both the dimensionless stiffness of the matrix, η, and the radius of the rod, r_r, but the dependence on the latter is found to be weak. As a result, we can further simplify Eq. (9) to

$$\frac{\lambda}{L_r} = \alpha\eta^{-1/4}, \qquad (10)$$

where the prefactor α is found to depend weakly on λ/r_r. For example, in our experiments where $134.4 < \lambda/r_r < 432.8$, the prefactor can be calculated to lie within $6.71 < \alpha < 7.04$. Given this limited range for α, and without loss of generality, for the reminder of this analysis we choose $\lambda/r_r = 240$, for which $\alpha = 6.88$. Note that an almost identical prediction for the wavelength (i.e. $\lambda/L_r = 6.62\eta^{-1/4}$) has been obtained using an energy approach and a nonlinear von Karman formulation to model the rod[26] (see SI for details).

In Fig. 4 B we plot the evolution of the dimensionless spring constant, $k = KL^4/(\pi E_r I_r)$, (left axis) and the buckling wavelength, λ, (right axis) as a function of the dimensionless matrix stiffness, η, determined by combining either Eqs. (7)* or (8) and (10). Using either the full version of K from Eq. (7) or its slender rod limit from Eq. (8), provide nearly identical predictions (solid lines and dashed lines, respectively) within the range of dimensionless matrix stiffness explored in this study. In Fig. 3B, the theoretical prediction for λ (black dashed line) is also superposed on top of our experimental results discussed above, showing excellent quantitative agreement.

In summary, our linear stability analysis is therefore able to correctly predict the experimentally observed buckling wavelength. Moreover, Eq. (6) indicates that, for certain values of k, two eigenmodes can be triggered simultaneously at the buckling onset, suggesting that the formation of non-planar buckling modes results form their interaction. This stability analysis is, however, unable to provide information on how these modes grow and interact. We now gain further insight into both of these effects through numerical simulations.

* The buckling wavelength λ associated to Eq. (7) has been calculated following a similar procedure to that reported above - see SI for details

4 Numerical Simulations

4.1 Discrete Elastic Rod simulations

We performed dynamic rod simulations using a code developed by Bergou *et al.*[29], where the response of an extensible Kirchhoff rod[30,31] under external forces is computed using a symplectic Euler method to update the position of the discretized system. More details on the code can be found in the original paper[29].

In our simulations, we matched the geometric and materials properties of the experimental Nitionol rods ($E_r = 64$ GPa, $r_r = 50\ \mu$m and $L_r = 9.7$ cm), with free rotation at both ends. Following the simplifications introduced in the theoretical description of §3, we modeled the confinement provided by the matrix as a series of linear springs with stiffness K given by Eq. (8), acting in the radial direction. A total of 22 rods were simulated, with different values of K; the exact value of the parameters for each analysis is provided in Table S2 of the SI.

In Fig. 5A and B we present two representative simulated buckling configurations for $k = KL^4/(\pi E_r I_r) = 2450$ and 1764, respectively. For the case of $k = 2450$, our analytical model from §3 predicts that the compressive forces associated with the first and second eigenmodes are well separated (see Eq. (6) and Fig. 4), which is consistent with the numerical finding that the rod buckles into a 2D planar configuration (Fig. 5A). By contrast, for $k = 1764$, Eq. (6) is satisfied with $m = 6$, such that the critical buckling forces associated with modes 6 and 7 are the lowest and identical. In this case, theory predicts that the rod should buckle into a non-planar 3D configuration. This is corroborated by the numerical configuration in Fig. 5B where modes 6 and 7 are triggered almost simultaneously and grow in two perpendicular lateral directions. We note that the rods that buckle into planar configurations may eventually deform into non-planar shapes because of a second bifurcation[32,33]. However, this transition occurs at strains much higher than those associated to the onset of the first instability, and is therefore beyond the scope of our study.

Similarly to the analysis of the experimental results discussed in §2, for each simulated configuration, we have also computed the ellipse of minimum area that encloses the cross-sectional projection of the rod.

In Fig. 5C we present the aspect ratio of this ellipse, b/a, as a function of the dimensionless spring constant k. For high values of the matrix stiffness ($k > 5000$), we find that $b/a \sim 1$ and the rod buckles in a non-planar configuration. On the other hand, for more moderate confinements ($k < 5000$), there is an alternation of 2D ($b/a \sim 0$) and 3D configurations as k is

View Article Online
DOI: 10.1039/C4SM00952E

increased. These numerical findings are in good agreement with the experimental results presented earlier in Fig. 2.

These dynamic simulations agree qualitatively with the experiments of §2, and support the stability analysis and subsequent interpretation presented in §3: the formation of 3D buckling configuration is due to the interactions between eigenmodes that are triggered nearly simultaneously. It is important to note, however, that in these dynamic simulations, similarly to the analytical model in §3, we have made the simplifying assumption that the elastomeric matrix is modeled as an array of linear springs that only act in the radial direction. In doing so, we have completely neglected the effect of shear of the distorted matrix, which we shall now see through finite element analysis becomes important past the onset of the buckling instability.

4.2 Finite element simulations

In order to more accurately capture the effect of the deformation of the elastomeric matrix on the response of the rod, we have performed finite element (FE) simulations of our system using the commercial package Abaqus. In these analyses the matrix was discretized using brick elements (Abaqus element type C3D8R) and, because of the small strains considered in this study, was modeled as a linear elastic material with Poisson's ratio $\nu_m = 0.495$. The rod was modeled as a beam (Abaqus element type B31) and assumed to be perfectly bonded to the matrix (using the embedded element algorithm available in Abaqus). The accuracy of the mesh was ascertained through a mesh refinement study, resulting in 11700 elements for the elastomeric matrix and 194 elements for the rod. In all FE simulations, we considered a rod with Young's modulus $E_r = 59$ GPa, radius $r_r = 101.5$ μm, length $L_r = 9.7$ cm and both ends were free to rotate. Moreover, the diameter of the matrix cylinder was chosen to be 2 cm, which was found to be sufficient to eliminate any boundary effects.

First, a buckling analysis was performed using a linear perturbation algorithm (through the `*BUCKLE` module in Abaqus). We carried out 50 simulations with the dimensionless matrix stiffness in the range $(0.54 < \eta < 2.69) \cdot 10^5$ to investigate its effects on the stability of the rod. In Fig. 6A we report the normalized separation between the lowest two critical forces, $\Delta f/f_{cr}$, as a function of η, where the FE results (blue continuous line) are compared with the previous analytical prediction (red dashed line). The corresponding dimensionless spring constant, k, calculated using Eq. (7) is also quantified on the upper horizontal axis. Both numerical and analytical results show the expected alternations of maxima and minima. However, there is a clear horizontal shift between the two sets of data. For example, in the region where theory predicts $n = 5$, we find $n = 4$ in the numerics and likewise for higher modes. This discrepancy indicates that although the simple Winkler foundation description does successfully provide a qualitative description of the response of the system, it is not sufficiently accurate to predict the exact conditions for which the rod will buckle into a 2D or 3D configuration. We speculate that the reasons for the differences between the reduced model (used in the analytical and the dynamic simulations) and the FE results is due to shear deformation in the matrix, which the Wrinkler model does not take into account.

Next, the post-buckling response was captured through dynamic explicit simulations, which were performed under quasi-static conditions ensured by monitoring the kinetic energy. In Fig. 6B and C we show two representative configurations recorded immediately after the buckling onset for two values of the dimensionless matrix stiffness $\eta = 1.30 \cdot 10^5$ and $8.40 \cdot 10^4$ (each marked in Fig. 6A by the points B and C, respectively). For $\eta = 1.30 \cdot 10^5$ a 2D buckling configuration is observed, as expected given that $\Delta f/f_{cr}$ is large in this case. In contrast, for $\eta = 8.40 \cdot 10^4$ a clear 3D buckling pattern emerges as the result of the interaction between two eigenmodes triggered nearly simultaneously, which grow in perpendicular directions. These FE results provide further confirmation that the dimensionless matrix stiffness determines whether the confined rod buckles into a 2D or 3D configuration by controlling the separation between the critical forces associated with the two lowest eigenmodes.

5 Discussion and conclusions

We have shown through a combination of experiments, theoretical analyses and numerical simulations that an elastic rod embedded within an elastomeric matrix can buckle into either a planar wavy configuration or a non-planar coiled configuration. Our analytical and numerical studies indicate that the separation $\Delta f/f_{cr}$ between the two lowest critical forces dictates the post-buckling behavior of the rod and that this parameter can be effectively controlled by changing the ratio between the stiffness of the matrix and the bending stiffness of the rod (i.e. the dimensionless matrix stiffness $\eta = E_m L_r^4/E_r I_r$). For large values of η the rod always buckles into a 3D coiled configuration, whereas for soft matrices, a monotonic increase of the stiffness results in an alternation between 2D planar and 3D coiled buckling configurations.

Good qualitative agreement was found between our analysis and experiments. However, a direct quantitative comparison is challenging due to the important role played by imperfections and measurement uncertainties. In fact, our analysis indicates that $\Delta f/f_{cr}$ is extremely sensitive to imperfections. For example, for a rod with $E_r = 59$ GPa, $L_r = 4$ cm, $r_r = 101.5$ μm embedded in a matrix with $E_m = 1.3$ kPa a relative uncertainty in the measurement of rod length and rod radius as small as 5% (i.e. $\Delta L_r/L_r \leq 5\%$ and $\Delta r_r/r_r \leq 5\%$) modifies the prediction of $\Delta f/f_{cr}$ from 0.28 to 0.021, leading to a switch from a

View Article Online
DOI: 10.1039/C4SM00952E

2D to a 3D buckling configuration.

Furthermore, we have also found that the buckling pattern is highly sensitive to the boundary conditions imposed at the two ends of the rod. In the experiments, small segments of the rod near its ends were embedded into a much stiffer disk to provide support and minimize rotation. In analysis and simulations, however, we assumed for the sake of simplicity that both ends of the rod were free to rotate.

To address this issue on the important role of the boundary conditions, we have repeated the stability analysis presented in §3 and the FE simulations in §4.2, but now also for rods whose ends are fixed (see SI for details). In Fig. 7A and B we present analytical and numerical (FE) results, respectively, for the evolution of the normalized separation between the two lowest critical forces as a function of the dimensionless matrix stiffness and compare the two cases of a rod with fixed and free-to-rotate ends. Both sets of results indicate that the profile of $\Delta f/f_{cr}$ for the case of a rod with fixed ends is shifted by approximately half a zone compared to that corresponding to a rod with free-to-rotate ends. By way of example, for a dimensionless stiffness of $k = 576$, our theory predicts that a confined rod buckles into a non-planar configuration if its ends are fixed, but into a planar configuration if the ends are free to rotate. Moreover, for the rod with fixed ends, the peaks of $\Delta f/f_{cr}$ are lower in magnitude and decreases considerably faster as a function of k, indicating a greater tendency to buckle into a 3D coiled shape, when compared to the rod with free-to-rotate ends. These results demonstrate that the boundary conditions at the extremities of the rod play an important role in determining the buckling shape. If the boundary conditions are not perfectly fixed in the experiments, we expect these uncertainties to have a significant influence on the final buckled configuration.

In conclusion, we have demonstrated that a rod embedded in an elastomeric matrix can buckle either into a planar (2D) or a non-planar (3D) configuration, in a way that depends non-trivially on the geometric and material parameters, as well as the boundary conditions. The 3D buckling configurations were rationalized to arise when two eigenmodes are triggered nearly simultaneously. Furthermore, our analysis indicate that the buckling pattern can be controlled by tuning both the matrix stiffness and the boundary conditions. This tunability, combined with the scalability of the buckling phenomenon, opens avenues for exploiting the underlying mechanical instabilities to generate the next generation of future photonic and piezoelectric devices with complex 3D structure. However, given the sensitivity of the system to imperfections, our study calls for more accurate fabrication protocols and experimental procedures to be able to exploit buckling as mechanism to generate complex patterns with fine tunable features.

Acknowledgement

We thank Eitan Grinspun and Da Fang for their help in setting up the rod dynamic simulations and Jibo Wen for the help with preliminary experiments. D.T. thanks the Belgian American Education Foundation (B.A.E.F.), the Fulbright Program and the Wallonie-Bruxelles International Excellence Grant W-BI.World. P.M.R. acknowledges financial support from the National Science Foundation (CMMI-1129894).

References

1 J. Lankford, *J. Maters. Sci.*, 1995, **30**, 4343-4348.
2 C. Bower, R. Rosen, L. Jin, J. Han and O. Zhou, *Appl. Phys. Lett.*, 1999, **74**, 3317.
3 R. Parnes and A. Chiskis, *J. Mech. Phys. Solids.*, 2002, **50**, 855-879.
4 M. Das, A. J. Levine and F. C. MacKintosh, *Europhys. Lett.*, 2008, **84**, 18003.
5 C. P. Brangwynne, F. C. MacKintosh, S. Kumar, N. A. Geisse, J. Talbot, L. Mahadevan, K. K. Parker, D. E. Ingber and D. A. Weitz, *J. Cell. Biol.*, 2006, **173**, 733-741.
6 L. R. Herrmann, W. E. Mason and S. T. K. Chan, *J. Compos. Mater.*, 1967, **1**, 212-226.
7 Y. Lanir and Y. C. B. Fung, *J. Compos. Mater.*, 1972, **6**, 387-401.
8 Y. Li, N. Kaynia, S. Rudykh and M. C. Boyce, *Adv. Eng. Mater.*, 2013, **15**, 921-926.
9 T. C. Maltby and C. R. Calladine, *Int. J. Mech. Sci.*, 1995, **37**, 943-963.
10 T. C. Maltby and C. R. Calladine, *Int. J. Mech. Sci.*, 1995, **37**, 965-983.
11 J. L. Silverberg, R. D. Noar, M. S. Packer, M. J. Harrison, C. L. Henley, I. Cohen and S. J. Gerbode, *Proc. Natl. Acad. Sci. U.S.A.*, 2013, **109**, 16794-16799.
12 W. S. Klug, M. T. Feldmann and M. Ortiz, *Comput. Mech.*, 2005, **35**, 146-152.
13 P. R. Paslay and D. B. Bogy, *J. Appl. Mech.*, 1964, **31**, 605-610.
14 T. Su, N. Wicks, J. Pabon, and K. Bertoldi, *Int. J. Solids. Struct.*, 2013, **50**, 2468-2476.
15 F. Xu, W. Lu and Y. Zhu, *ACS Nano*, 2011, **5**, 672-678.
16 X. Y. Kong and Z. L. Wang, *Nano Lett.*, 2003, **3**, 1625-1631.
17 X. Chen, S. Zhang, D. A. Dikin, W. Ding, R. S. Ruoff, L. Pan and Y. Nakayama, *Nano Lett.*, 2003m **3**, 1299-1304.
18 M. A. Poggi, J. S. Boyles, L. A. Bottomley, A. W. McFarland, J. S. Colton, C. V. Nguyen, R. M. Stevens and P. T. Lillehei, *Nano Lett.*, 2004, **4**, 1009-1016.
19 S. P. Timoshenko and J. M. Gere, *Theory of Elastic Stability*, McGraw-Hill, 2nd ed., 1961.
20 D. C. Lagoudas, *Shape Memory Alloys: Modeling and Engineering Applications* , Springer, 2010.
21 D. Stoeckel and W. Yu, *Wire J. Int.*, 1991, **24**, 45-50.
22 F. Brau, H. Vandeparre, A. Sabbah, C. Poulard, A. Boudaoud and P. Damman, *Nat. Phys.*, 2011, **7**, 56-60.
23 W. Shan, Z. Chen, C. P. Broedersz, A. A. Gumaste, W. O. Soboyejo and C. P. Brangwynne, *Soft Matter*, 2013, **9**, 149-199.
24 I. T. Jolliffe, *Principal Component Analysis*, Springer, 2nd ed., 2002.
25 M. Ringnér, *Nat. Biotechnol.*, 2008, **28**, 303-304.
26 H. Jiang and J. Zhang, *J. Appl. Mech.*, 2008, **75**, 061019.
27 J. Wu, Z. J. Liu, J. Z. Song, Y. Huang, K-C. Hwang, Y. W. Zhang, J. A. Rogers, *Applied Physics Letters*, 2011, **99**, 61911.
28 E. Byskov and J. W. Hutchinson, *AIAA Journal*, 1977, **15**, 941-948.
29 M. Bergou, M. Wardetzky, S. Robinson, B. Audoly and E. Grinspun, *ACM T. Graphic.*, 2008, **27**, 63.

View Article Online
DOI: 10.1039/C4SM00952E

30 G. Kirchhoff, *J. f. Reine Angew. Math.*, 1859, **56**, 285-313.
31 G. Kirchhoff, *Vorlesungen über mathematische Physik*, Mechanik, 1876.
32 G. H. M. Van der Heijden, S. Neukirch, V. G. A. Goss, J. M. T. Thompson, *Int. J. Mech. Sci.*, 2003, **45**, 161-196.
33 S. Goyal, N. C. Perkins, C. L. Lee, *J. Comput. Phys.*, 2005, **209**, 371-389.

View Article Online
DOI: 10.1039/C4SM00952E

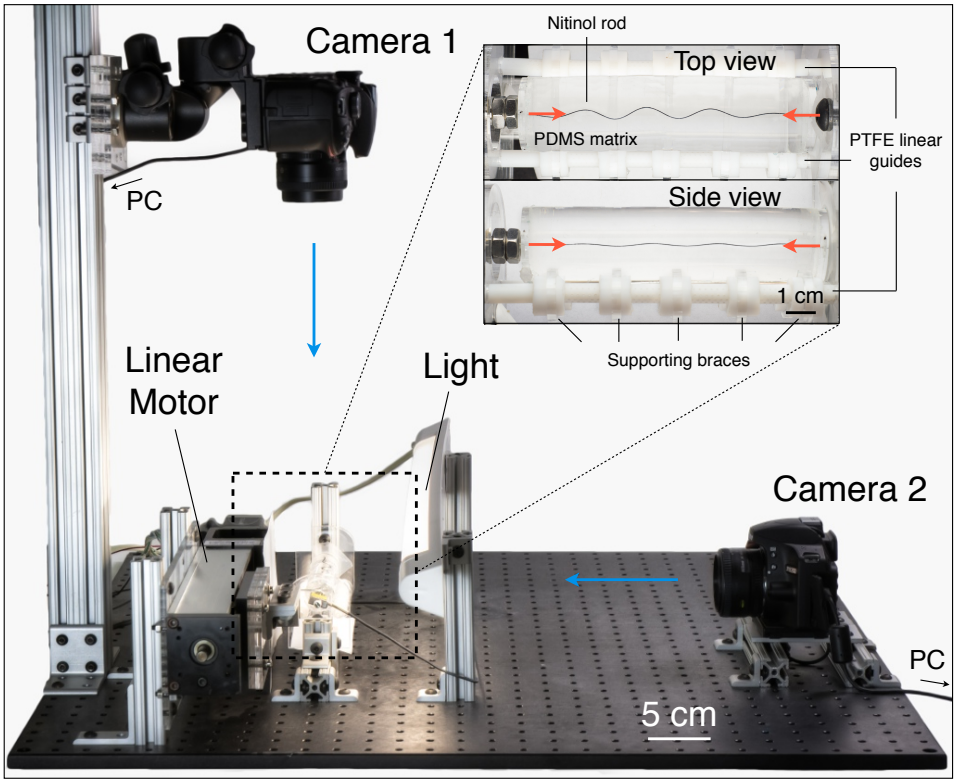

Fig. 1 Experimental apparatus. A Nitinol rod is embedded within a cylindrical PDMS matrix (inside dashed frame). The sample is uniaxially compressed under displacement control. Two synchronized cameras placed on the top and side of the setup capture snapshots of the buckling of the rod (insets). The paired images are then sent to a computer for reconstruction of the configuration of the rod and further analyses.

View Article Online
DOI: 10.1039/C4SM00952E

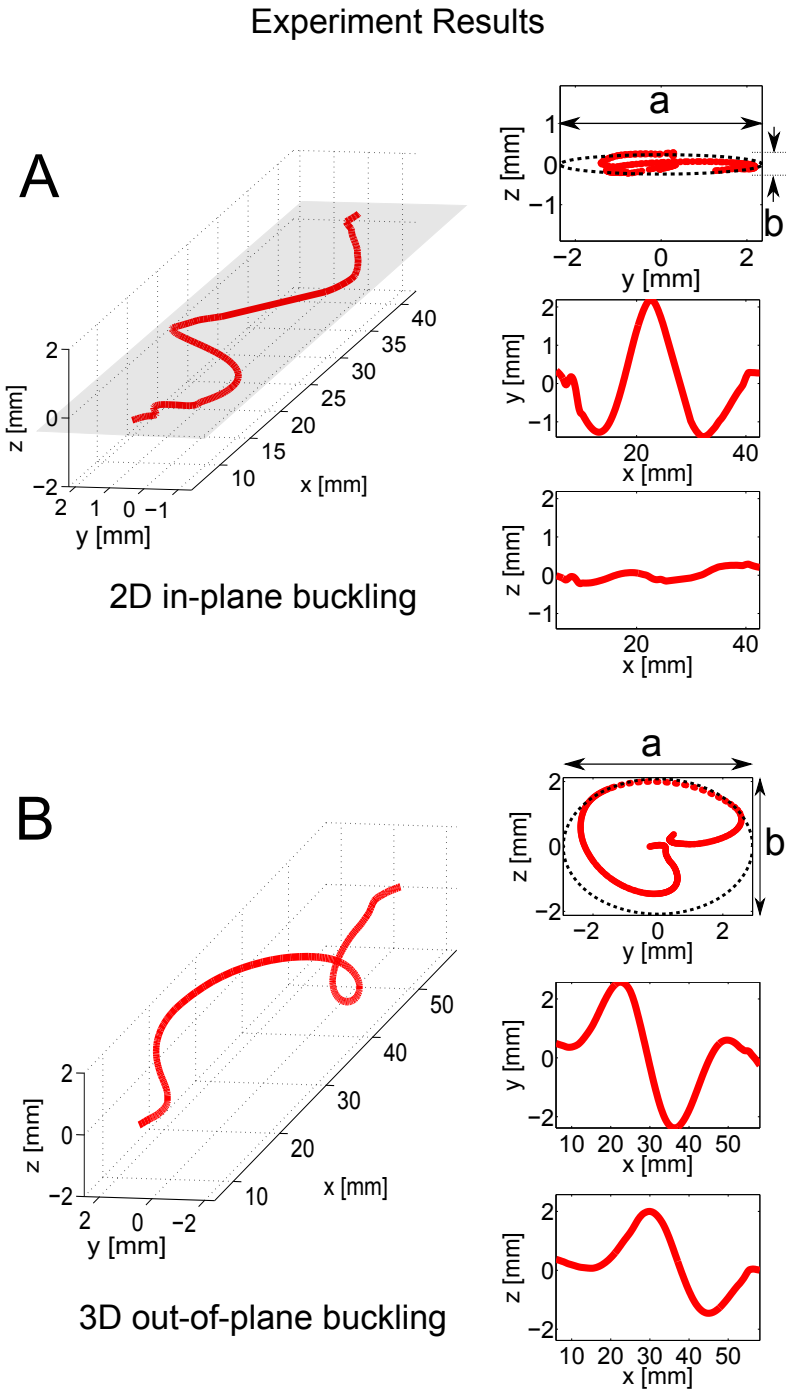

Fig. 2 Experimental results. Buckled configurations of (A) Sample #1 and (B) Sample #2 acquired at $\varepsilon = 3\%$ compressive strain. Both 3D and projected views (onto the *z*-*y*, *y*-*x* and *z*-*x*) are shown, clearly indicating that Sample #1 buckles into a 2D planar configurations, while Sample #2 buckles into a 3D coiled configuration. The dashed ellipse shown in the y-z view corresponds to the ellipse with minimum area that encloses the cross-sectional projection of the rod..

View Article Online
DOI: 10.1039/C4SM00952E

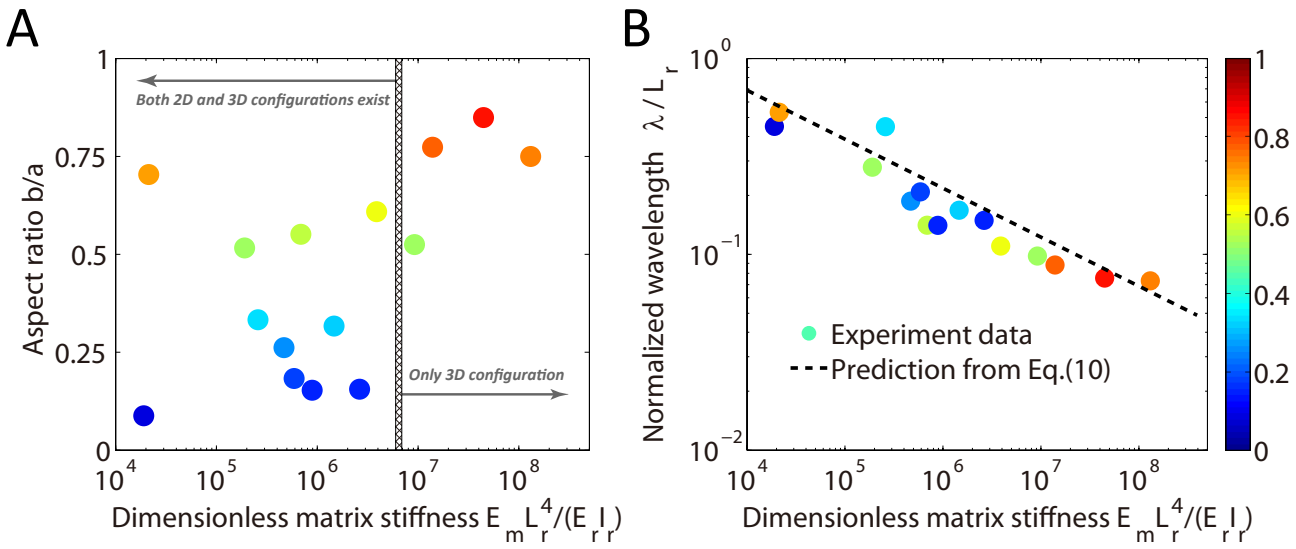

Fig. 3 Characteristic length scales of the buckled samples. (A) Ratio between the minor and major axes of the minimum area ellipse that encloses the cross-sectional view at $\varepsilon = 3\%$ as a function of the normalized matrix stiffness $\eta = E_m L^4/(E_r I_r)$. Small b/a values indicate a planar buckling configuration, while large values of b/a correspond to 3D coiled configurations. (B) Normalized buckling wavelength λ/L_r as a function of the normalized matrix stiffness η. Excellent agreement is found between the experimental results (data points) and the analytical prediction (dashed black line - Eq. 10) obtained using the Winkler foundation model. The color of the markers indicates the corresponding b/a value for each sample, as given by the adjacent color bar.

View Article Online
DOI: 10.1039/C4SM00952E

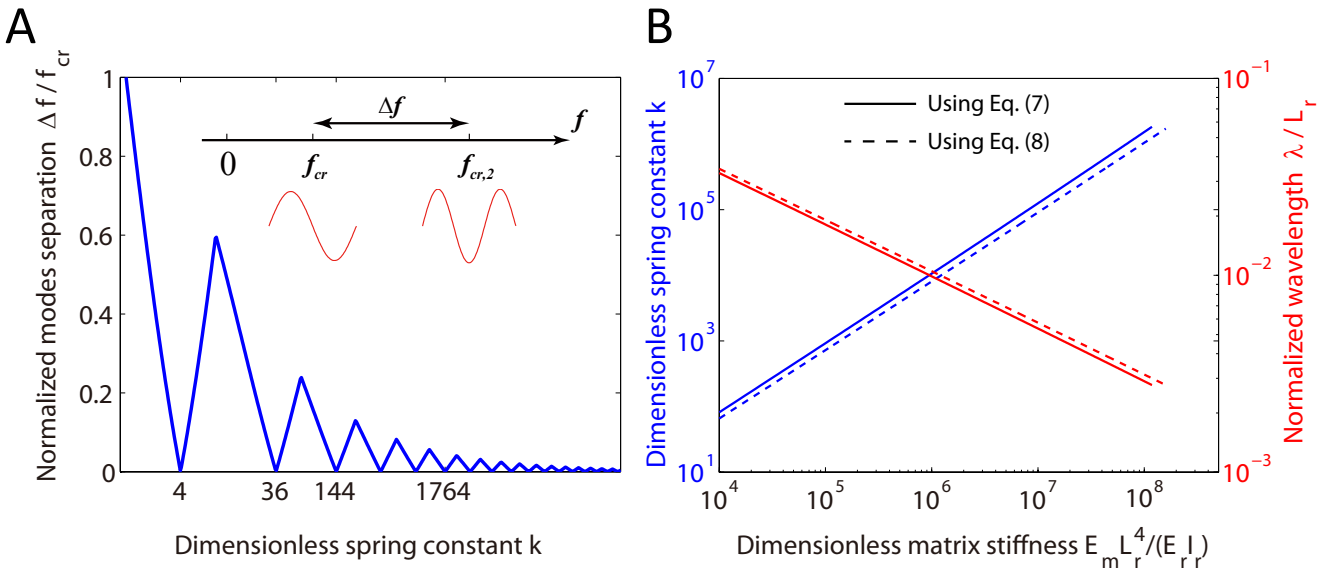

Fig. 4 Theoretical results. (A) Normalized separation of the critical forces associated with the two lowest modes, $\Delta f/f_{cr}$, as a function of the dimensionless matrix spring constant k. The Winkler foundation model as been used and the rod has free-to-rotate ends. For some specific values of k (provided by Eq. (6)) $\Delta f = 0$, so that two modes are triggered simultaneously at the buckling onset. (B) Dimensionless spring constant k (blue lines) and wavelength λ/L_r (red lines) as function of $\eta = E_m L_r^4/(E_r I_r)$ for a rod with radius $r_r = 101.5\,\mu$m. Solid and dashed lines correspond to the prediction obtained using Eqs. (7) and (8), respectively.

View Article Online
DOI: 10.1039/C4SM00952E

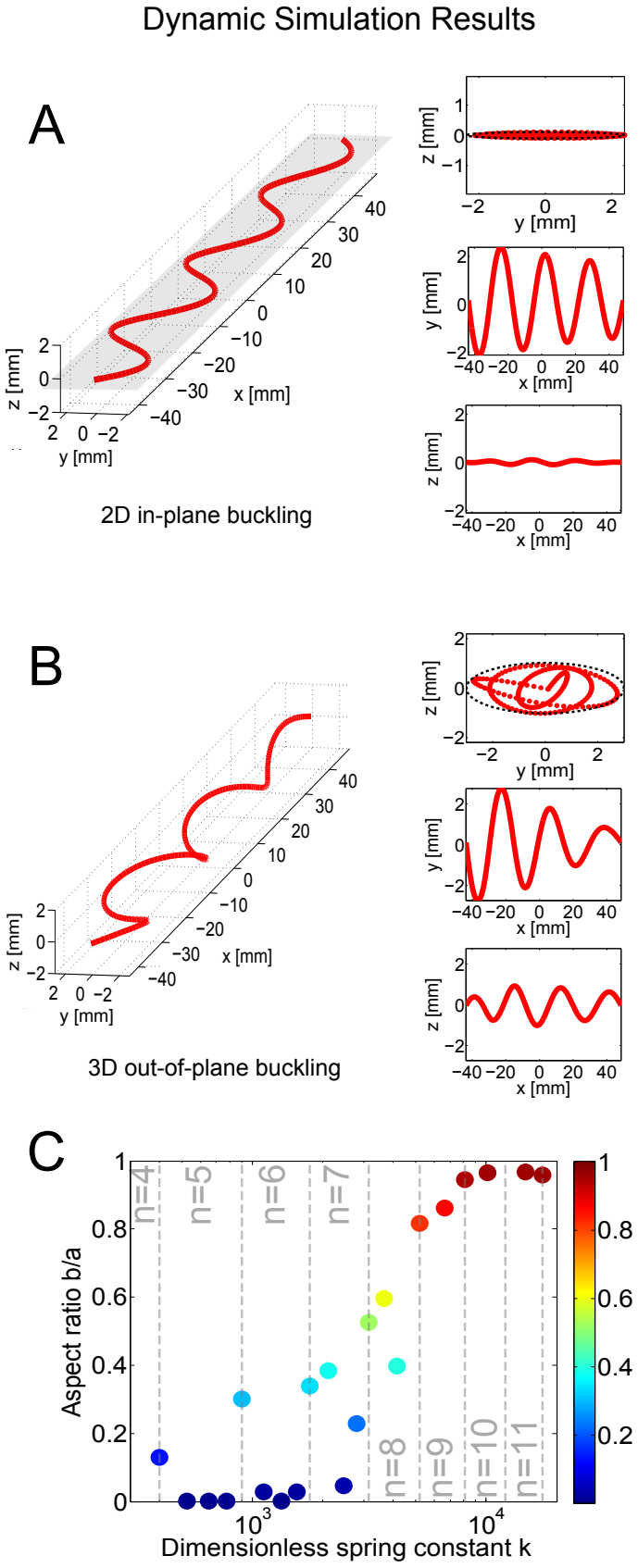

Fig. 5 Discrete elastic rod simulations. (A-B): Buckling configuration for (A) k = 2450, and (B) k = 1764. (C) Ratio between the minor and major axes b/a of the minimum area ellipse that encloses the rod cross sectional view as a function of dimensionless spring constant k. The critical $k = n^2 (n+1)^2$ where two modes are expected to occur simultaneously are shown in vertical lines.

View Article Online
DOI: 10.1039/C4SM00952E

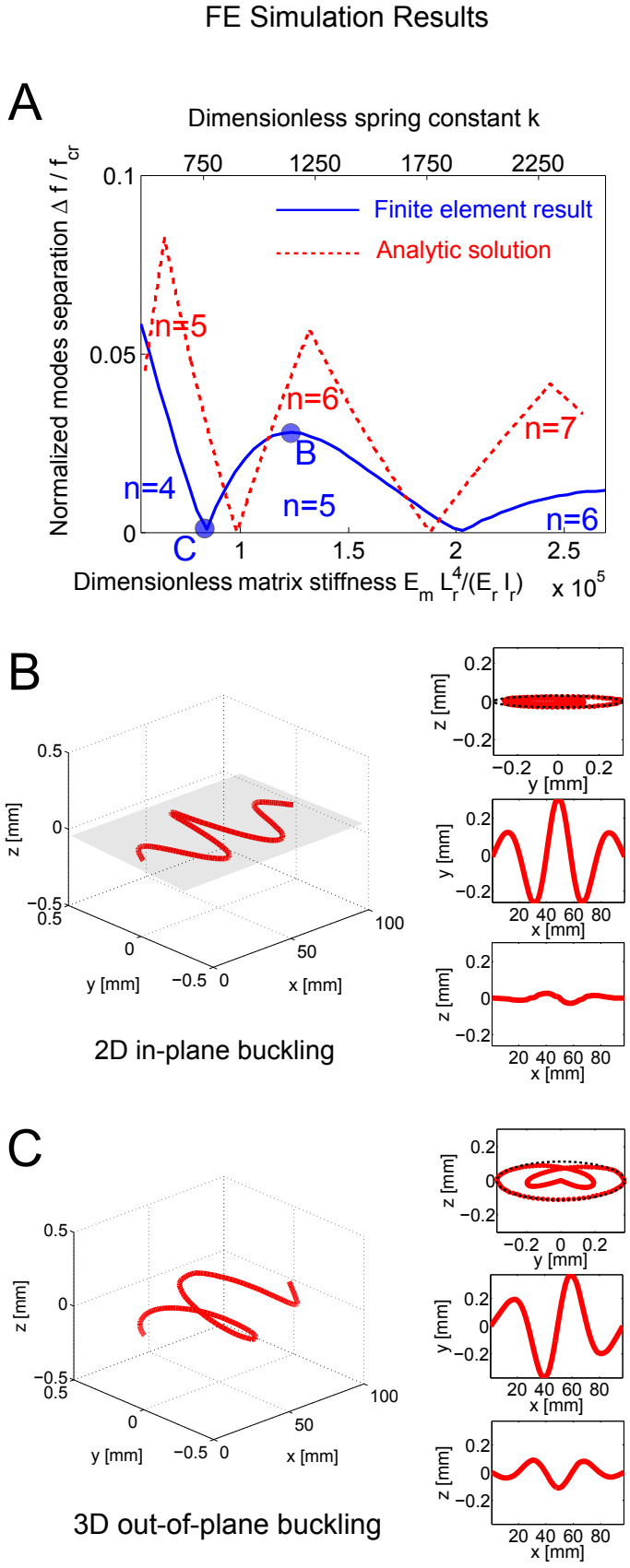

Fig. 6 Finite element (FE) results. (A) Normalized separation of the critical forces associated with the two lowest modes, $\Delta f/f_{cr}$, as a function of k (bottom) and the dimensionless matrix stiffness η (top) predicted by the theory (red line) and FE simulations (blue line). (B-C) Configurations recorded immediately after the buckling onset for systems with $\eta = 1.30 \cdot 10^5$ and $8.40 \cdot 10^4$, corresponding to markers A and B in (A).

View Article Online
DOI: 10.1039/C4SM00952E

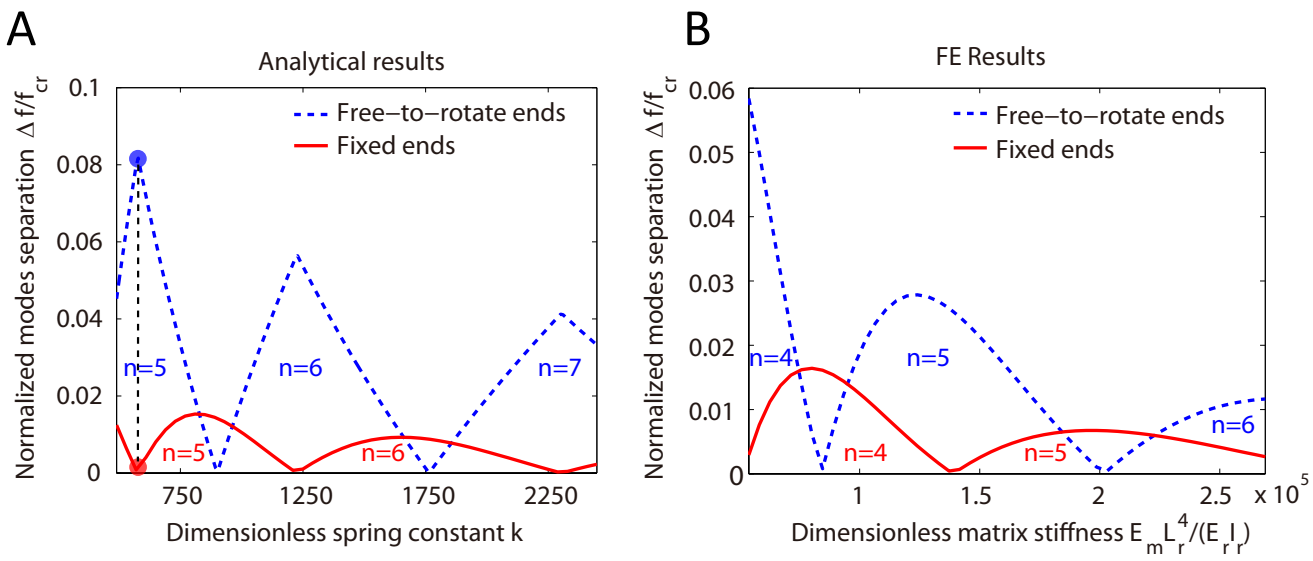

Fig. 7 Effect of boundary conditions. (A) Analytical predictions for the normalized separation of the critical forces associated with the two lowest modes, $\Delta f / f_{cr}$, as function of k for a rod with free-to-rotate (blue line) and fixed (red line) ends. (B) FE predictions for the normalized separation of the critical forces associated with the two lowest modes, $\Delta f / f_{cr}$, as function of η for a rod with free-to-rotate (blue line) and fixed (red line) ends.